

VLBI astrometry on the white dwarf pulsar AR Scorpii

Pengfei Jiang,^{1,2} Lang Cui^{1,3*}, Jun Yang^{1,4}, Bo Zhang,⁵ Shuangjing Xu,^{5,6} Fengchun Shu^{1,5},
Wu Jiang,⁵ Wen Chen^{1,2,7}, Guanghui Li,¹ Bo Xia,⁵ Stuart Weston,⁸ Sergei Gulyaev,⁸ Hongmin Cao,⁹
Xiang Liu^{1,3} and Tao An^{1,5}

¹Xinjiang Astronomical Observatory, Chinese Academy of Sciences, 150 Science 1-Street, 830011 Urumqi, P. R. China

²School of Astronomy and Space Science, University of Chinese Academy of Sciences, 100049 Beijing, P. R. China

³Key Laboratory of Radio Astronomy, Chinese Academy of Sciences, 150 Science 1-Street, 830011 Urumqi, P. R. China

⁴Department of Space, Earth and Environment, Chalmers University of Technology, Onsala Space Observatory, SE-439 92 Onsala, Sweden

⁵Shanghai Astronomical Observatory, Chinese Academy of Sciences, 200030 Shanghai, P. R. China

⁶Korea Astronomy and Space Science Institute, 776 Daedeokdae-ro, Yuseong-gu, Daejeon 34055, Republic of Korea

⁷Yunnan Observatories, Chinese Academy of Sciences, 650216 Kunming, Yunnan, P.R. China

⁸Institute for Radio Astronomy and Space Research, Auckland University of Technology, Private Bag 92006, Auckland 1142, New Zealand

⁹School of Electronic and Electrical Engineering, Shangqiu Normal University, Wenhua Road 298, Shangqiu, Henan 476000, P. R. China

Accepted 2023 January 25. Received 2023 January 24; in original form 2022 May 3

ABSTRACT

AR Scorpii (AR Sco), the only-known radio-pulsing white dwarf binary, shows unusual pulsating emission at the radio, infrared, optical, and ultraviolet bands. To determine its astrometric parameters at the radio band independently, we conducted multi-epoch Very Long Baseline Interferometry (VLBI) phase-referencing observations with the European VLBI Network at 5 GHz and the Chinese VLBI Network plus the Warkworth 30-m telescope (New Zealand) at 8.6 GHz. By using the differential VLBI astrometry, we provide high-precision astrometric measurements on the parallax ($\pi = 8.52_{-0.07}^{+0.04}$ mas) and proper motion ($\mu_\alpha = 9.48_{-0.07}^{+0.04}$ mas yr⁻¹, $\mu_\delta = -51.32_{-0.38}^{+0.22}$ mas yr⁻¹). The new VLBI results agree with the optical *Gaia* astrometry. Our kinematic analysis reveals that the Galactic space velocities of AR Sco are quite consistent with that of both intermediate polars and polars. Combined with the previous tightest VLBI constraint on the size, our parallax distance suggests that the radio emission of AR Sco should be located within the light cylinder of its white dwarf.

Key words: techniques: high angular resolution – parallaxes – pulsars: individual: AR Sco – white dwarfs – radio continuum: stars.

1 INTRODUCTION

AR Scorpii (AR Sco) is a white dwarf (WD)/M-type star binary with an orbital period of ~ 3.56 h and a WD spin period of ~ 1.95 min (Marsh et al. 2016). Unusual pulsations in short time-scales of a period of ~ 1.97 min are detected at multiple bands (ultraviolet, optical, infrared, and radio). Its non-synchronous spin and orbital periods imply a connection with a class of stars known as intermediate polars (IPs; e.g. Patterson 1994), whereas its weak X-ray radiation distinguishes itself from usual IPs (Takata et al. 2018). The strong radio emission and broad-band spectral energy distribution of AR Sco are similar to those of a special IP system AE Aquarii (Bookbinder & Lamb 1987; Oruru & Meintjes 2012). However, the radio pulsation properties of AR Sco were unique among WD systems.

The exact emission mechanism of AR Sco is still unclear and a large number of models have been proposed to interpret its unique observed behaviour. Marsh et al. (2016) proposed scenarios where the pulsed emission came from collimated fast particle outflows or the direct interaction of the magnetosphere of the WD with the M companion. Geng, Zhang & Huang (2016) suggested that the WD's rotational axis was nearly perpendicular to its magnetic axis,

and the magnetic interaction occurred when the WD's open field line beams swept the secondary's wind. Katz (2017) also proposed a misaligned-spin model and supposed a precessing spin axis to explain the displacement of the optical maximum from conjunction of this system, but suggested that the magnetic interaction occurs within the MD's atmosphere. Garnavich et al. (2019) investigated the possible existence of magnetic loops or prominence of the M star, the magnetic interaction with these may contribute to the system's emission. The energy that comes from AR Sco may be generated through magnetohydrodynamic interactions (Buckley et al. 2017) or fast magnetic reconnection events (Garnavich et al. 2019), and Bednarek (2018) discussed a hadronic model.

Accurate astrometry on AR Sco will allow us to constrain its physical properties (e.g. velocity, luminosity, emission region size). It helps to validate the theoretical models, to trail the evolutionary history, and to explore the possibility of this system being a future source of detectable gravitational wave emission (Franz & Schramm 2017). For AR Sco, Marsh et al. (2016) gave a rough estimate of the distance of $d = 116 \pm 16$ pc, based on the spectra and photometry of the M star in optical and infrared. By combining with the first *Gaia* Data Release (Gaia Collaboration 2016), the fifth US Naval Observatory CCD Astrograph Catalog (Zacharias, Finch & Frouard 2017) obtained a proper motion estimate of $\mu_\alpha = 4.0 \pm 2.2$ mas yr⁻¹, $\mu_\delta = -50.8 \pm 2.0$ mas yr⁻¹ in optical. Based

* E-mail: cuilang@xao.ac.cn

Table 1. Summary of VLBI observations of AR Sco.

Project Code	Date	Freq. (GHz)	Participating stations ^a	Duration (h)	Detection
EL058A	2017 Feb 15	5.0	Ef, Jb, Mc, Nt, O8, Tr, Ys, Wb, Hh	4.4	No
EL058B	2017 Apr 12	5.0	Jb, Mc, Nt, O8, Tr, Ys, Wb, Hh, Ib	4.0	Yes
EL058C	2017 Jun 20	5.0	Ef, Jb, Mc, Nt, Tr, Ys, Wb, Hh, Ir	4.0	Yes
EL058D	2017 Sep 19	5.0	Ef, Jb, Nt, O8, Tr, Ys, Wb, Hh, Ir	3.8	Yes
EL058E	2018 Jan 17	5.0	Ef, Jb, Mc, Nt, O8, Tr, Hh, Ir	3.9	No
CC001A	2017 Sep 25	8.6	Sh, T6, Km, Ur, Wa	6.5	No
CC001B	2017 Dec 19	8.6	Sh, T6, Km, Ur, Wa	6.2	Yes
CC001C	2018 May 11	8.6	Sh, T6, Km, Ur, Wa	6.8	Yes
CC001D	2018 Jul 30	8.6	Sh, Km, Ur, Wa	6.9	No
CC001E	2018 Sep 13	8.6	T6, Km, Ur	6.9	Yes

Note. ^aEf: Effelsberg (100 m), Jb: Jodrell Bank MKII (38 × 25 m), Mc: Medicina (32 m), Nt: Noto (32 m), O8: Onsala-85 (25 m), Tr: Torun (32 m), Ys: Yebes (40 m), Wb: Westerbork (25 m), Hh: Hartebeesthoek (26 m), Ir: Irbene (32 m), Ib: Irbene (16 m), Sh: Shanghai (25 m), T6: Tianma (65 m), Km: Kunming (40 m), Ur: Urumqi (26 m), Wa: Warkworth (30 m).

on optical astrometric measurements, the *Gaia* Early Data Release 3 (*Gaia* EDR3; Gaia Collaboration 2021) provided a parallax estimate of $\pi = 8.544 \pm 0.038$ mas and proper motion estimates of $\mu_\alpha = 9.690 \pm 0.047$ mas yr⁻¹, $\mu_\delta = -51.489 \pm 0.038$ mas yr⁻¹ for AR Sco. Our goal was to determine the astrometric parameters of AR Sco with the technique of Very Long Baseline Interferometry (VLBI) at the radio band. As the only technique that can derive high precision positions of target sources comparable to *Gaia*, VLBI could provide new and independent astrometric results to validate the *Gaia* results.

In this paper, we present new astrometric measurements for AR Sco from the European VLBI Network (EVN) and the Chinese VLBI Network (CVN) plus Warkworth 30-m radio telescope observations over a period of ~ 1.5 yr. We describe the observations and data reduction in Section 2. The high-precision astrometric results are presented in Section 3. We compare our VLBI results with those from *Gaia*'s, and analyse the kinematics and physical parameters of AR Sco in Section 4. Finally, we summarize the study in Section 5.

2 OBSERVATIONS AND DATA REDUCTION

2.1 EVN observations and data reduction

Our EVN observations of AR Sco at 5 GHz were conducted in e-VLBI mode (Szomoru 2009) at five epochs between 2017 February and 2018 January. Table 1 lists the observing dates, the participating stations, and the time durations. The raw data were at a data rate of 2048 Mbps (dual polarization, 8×32 MHz bandwidth per polarization, two-bit quantization) and correlated in real time (e-EVN mode) by the SFXC software correlator (Keimpema et al. 2015) at JIVE (Joint Institute for VLBI ERIC, the Netherlands).

The observations of AR Sco were performed with the two phase-referencing calibrators: PKS J1625–2527 (J1625–2527; e.g. Fey, Clegg & Fomalont 1996) and PMN J1621–2241 (J1621–2241; Griffith et al. 1994). The primary calibrator J1625–2527 located 2:7 away from AR Sco was selected from *Astroge Centre*.¹ The secondary calibrator J1621–2241 was selected based on our pilot short VLBI observation (project code: RSC03) at 5 GHz. It is 12 arcmin away from AR Sco, and shows a point-like structure with a peak brightness of ~ 20 mJy beam⁻¹. The cycle time was about 6 min: ~ 1 min for the primary calibrator, ~ 4 min for the target, and ~ 1 min for the gap. The secondary calibrator was observed for one

Table 2. Source correlation phase centres. θ_{sep} give source separations from AR Sco.

Source	α (J2000)	δ (J2000)	θ_{sep}
AR Sco ^a	16 ^h 21 ^m 47 ^s .303367	−22°53′11″.46486	...
J1625–2527 ^b	16 ^h 25 ^m 46 ^s .891639	−25°27′38″.32688	2:7
J1621–2241	16 ^h 21 ^m 32 ^s .276276	−22°41′01″.40904	0:2

Note. ^aThe correlation phase centre is only for EL058B. ^bThe position was taken from <http://astrogeo.org/vlbi/solutions/rfc.2015a/>.

~ 2 min scan per three cycles. This additional faint calibrator allows us to run a further iteration of the phase-referencing calibration to significantly improve the astrometric precision (e.g. Doi et al. 2006; Paragi et al. 2013). Table 2 lists the correlation phase centres for these three sources.

The data reduction was performed with the NRAO Astronomical Image Processing System (AIPS; Greisen 2003). The baselines when one or both antennas were pointing below 10° elevation or the data were severely corrupted by radio frequency interference, weather, recording, or instrumental problems were initially flagged. No correction was made to update the Earth Orientation Parameters or digital sampling bias corrections applied at correlation time by the SFXC correlator. The ionospheric delay was corrected using Jet Propulsion Laboratory Global Ionospheric Maps with the AIPS task TECOR. We conducted a priori amplitude calibration via standard gain curves and system temperature measurements of participating stations. In case of no available system temperature data, the priori amplitude calibration was conducted using the nominal system equivalent flux densities with the AIPS task CLCOR. The parallactic angle correction was applied by the task CLCOR. The instrumental phase errors across intermediate frequencies were removed through a manual phase calibration with the primary calibrator J1625–2527. Global fringe fitting and bandpass calibration were also applied with J1625–2527. The AIPS task CALIB was used to compute both amplitude and phase self-calibration corrections for J1625–2527, and the solutions were transferred to the secondary calibrator J1621–2241 and the target AR Sco. After these calibrations, the phases of both J1621–2241 and AR Sco were phase referenced to J1625–2527. Imaging and self-calibration for J1621–2241 data were performed in DIFMAP (Shepherd, Pearson & Taylor 1994). The clean maps for J1621–2241 without self-calibration were then loaded into AIPS, and the position and position uncertainties were derived with the task JMFIT. In our experiments, the secondary calibrator J1621–2241

¹<http://astrogeo.org/calib/search.html>

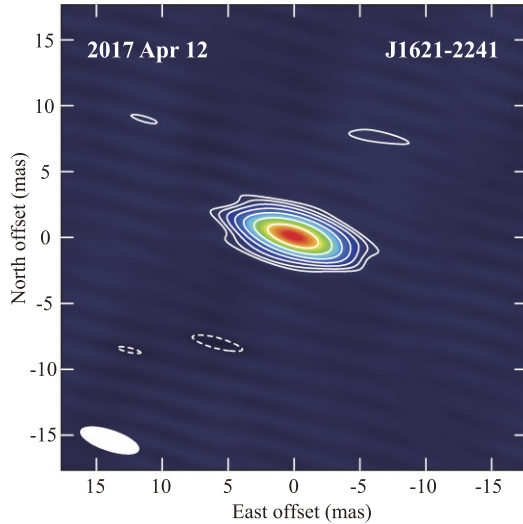


Figure 1. The EVN 5 GHz image of the secondary phase-referencing calibrator J1621–2241. The image was obtained with natural weighting and self-calibration. The contours start from $0.3 \text{ mJy beam}^{-1}$ and increase by a factor of two. The synthesized beam is plotted as the white ellipse in the bottom left corner and has a full width at half-maximum (FWHM) of $4.6 \times 1.5 \text{ mas}^2$ at position angle $\text{PA} = 71.8^\circ$.

was regarded as a stationary reference source. We set J1621–2241 at its correlation phase centre with a point model and used the AIPS task CALIB to derive phase corrections, and the corresponding solutions were applied to J1621–2241 and AR Sco. This step could improve the final image fidelity of AR Sco. And AR Sco was phase referenced to J1621–2241. Finally, we imaged AR Sco in AIPS.

2.2 CVN plus wa observations and data reduction

In order to expand the time span of the observations and improve astrometric accuracy, we also conducted VLBI observations of AR Sco at 8.6 GHz with the CVN plus the Warkworth 30-m radio telescope (Wa; Woodburn et al. 2015), located in New Zealand, under the program CC001 at five epochs between 2017 September and 2018 September. Adding Wa to the network allowed us to significantly boost the resolution in the north–south direction. The observing setup is also summarized in Table 1. The data were recorded in the discs at a data rate of 2048 Mbps (16 subbands, 32 MHz filters, right-hand circular polarization, two-bit quantization). The correlation was executed with the DIFX software correlator (Deller et al. 2011) at Shanghai Astronomical Observatory.

These CVN plus Wa observations at 8.6 GHz followed the above EVN observing strategy. The data were also reduced and imaged in a very similar way. Moreover, the EOPs and digital sampler bias corrections were performed with the AIPS task CLCOR and ACCOR, respectively.

3 RESULTS

3.1 VLBI imaging results

The EVN image of the secondary calibrator J1621–2241 observed on 2017 April 12 is shown in Fig. 1. This image was made with natural weighting and has a noise level of $0.3 \text{ mJy beam}^{-1}$. It shows a point-like source with a peak flux density of $36.4 \text{ mJy beam}^{-1}$. Fitting a circular Gaussian model to the visibility data gave a flux density of

$\sim 41.3 \text{ mJy}$ and a size of $\sim 0.7 \text{ mas}$. For CVN plus Wa observations at 8.6 GHz, the calibrator also shows a point-like source with a mean total flux density of $\sim 40.6 \text{ mJy}$ and a mean size of $\sim 1.2 \text{ mas}$.

Fig. 2 shows the CLEAN maps of the WD pulsar AR Sco at 5 GHz in the top panels and at 8.6 GHz in the bottom panels. All the images were produced with natural weighting. AR Sco displays an unresolved structure at all epochs. Fitting a circular Gaussian model to the visibility data from the highest SNR epoch EL058B gave a size of $1.6 \pm 0.1 \text{ mas}$ for AR Sco. The related information is listed in Table 3. The images have relatively higher noise levels than the estimated thermal noise, especially for (c) and (f) listed in Table 3, probably due to a significant sensitivity loss of the 32 MHz digital filters of the digital base band converter 2 system (DBBC2), which was also reported in other EVN observations at similar period (e.g. Yang et al. 2020). To get more reasonable flux density estimates, we scaled the amplitudes by a factor of 1.7 and took a large fraction, 15 percent, of the flux density as the uncertainty in Table 3. The factor was derived by comparing our flux densities obtained from CVN observations at 8.6 GHz with that obtained from the Australian Long Baseline Array (LBA) observation at 8.4 GHz (Marcote et al. 2017).

The target AR Sco were successfully detected in six epochs. In the other four epochs (EL058A, EL058E, CC001A, CC001D), there were no useful astrometric results because of various issues (antenna failures, weak/no fringes for the calibrators, low observing elevations, and incorrect coordinate).

3.2 Astrometry

The position of the extragalactic reference source J1621–2241 was obtained from both the EVN observations and the CVN plus Wa observations, with respect to the primary calibrator J1625–2527. We found that the position dispersion in the EVN observations ($\sigma_\alpha = 9.8 \text{ mas}$, $\sigma_\delta = 8.9 \text{ mas}$) was larger than that in the CVN plus Wa observations ($\sigma_\alpha = 1.0 \text{ mas}$, $\sigma_\delta = 1.8 \text{ mas}$). For the EVN observations, the relatively high latitude of the array caused the difficulty of observing such low declination source, the majority of antennas were pointing at relatively low elevation ($\sim 15^\circ$) during observations. The large angular distance between the primary calibrator and the secondary could lead to lobe ambiguities for these low elevation observations. The limited on-source time ($\sim 20 \text{ min}$) for the secondary calibrator could aggravate this condition. These terms cause the large position dispersion for J1621–2241 in the EVN observations. For the CVN plus Wa observation, the relative lower latitude array and longer on-source time ($\sim 1 \text{ h}$) for J1621–2241 alleviate this problem. Moreover, the lobe ambiguities will be eliminated for the target when referencing the target to the secondary calibrator, as the secondary calibrator is only 12 arcmin away from the target.

A weighted average method was used to derive the position of J1621–2241 with the combination of EVN observations and CVN plus Wa observations. First, the arithmetic mean position was calculated from each of the two observational arrays separately. Next, we derived the weighted mean position from the two arithmetic mean positions. The weights of the mean positions from two arrays were set as inversely proportional to the square of their dispersion. As the used calibrator J1625–2527 is an International Celestial Reference Frame (ICRF) defining source, its position was corrected by its ICRF3² (Charlot et al. 2020)

²<https://hpiers.obspm.fr/icrs-pc/newwww/index.php>

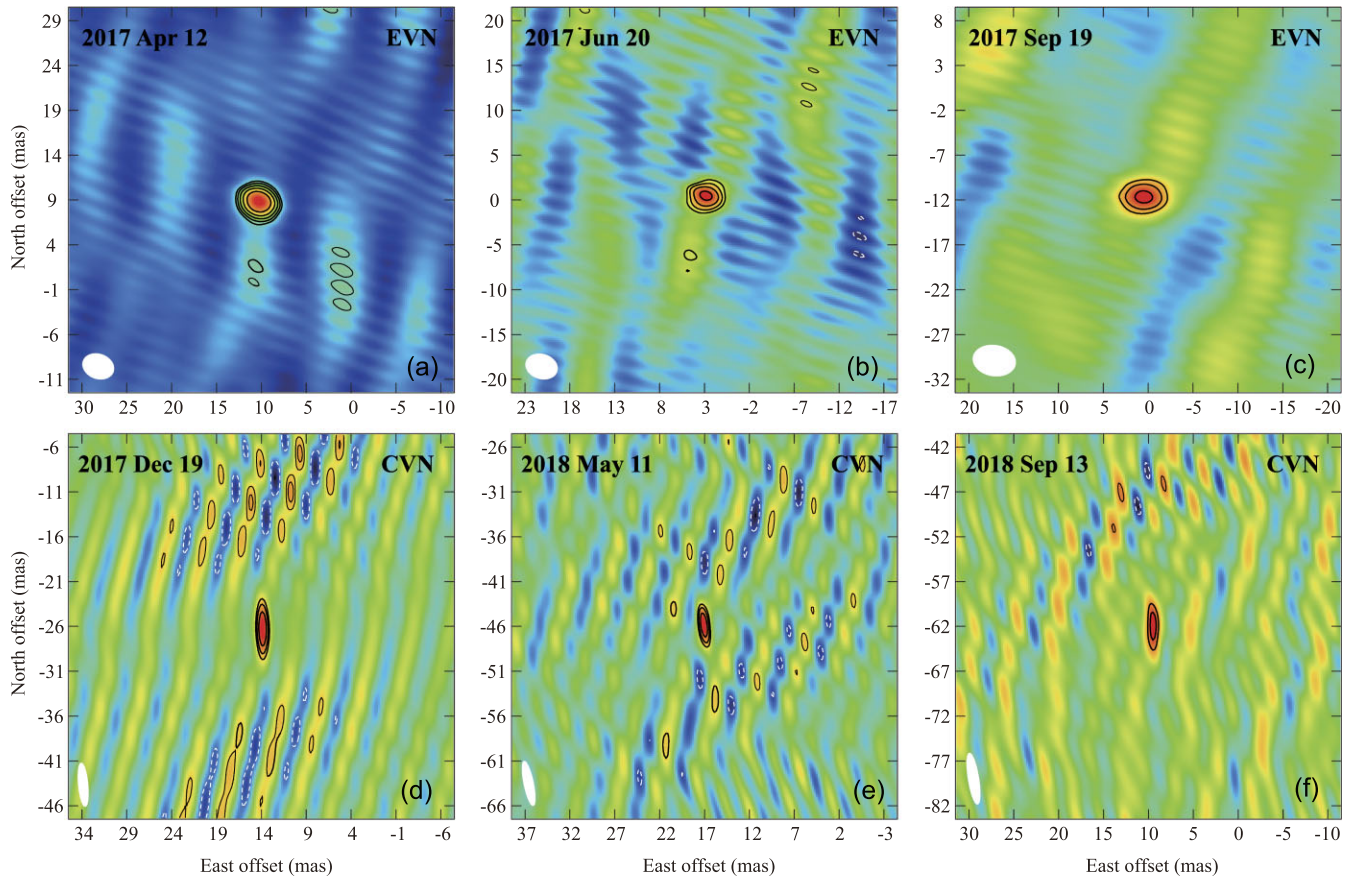


Figure 2. The VLBI CLEAN maps of the WD pulsar AR Sco at 5 GHz (top) and 8.6 GHz (bottom). The synthesized beam is shown in the bottom left corner of each panel. Contours start at three times the noise level of images and increase by factors of $\sqrt{2}$. The related information is listed in Table 4.

Table 3. Summary of VLBI imaging results of AR Sco^a.

Panel	MJD (d)	FWHM (mas)	PA ($^{\circ}$)	$S_{5\text{GHz}}$ (mJy beam $^{-1}$)	$S_{8.6\text{GHz}}$ (mJy beam $^{-1}$)	SNR	$\Delta\alpha\cos\delta$ (mas)	$\Delta\delta$ (mas)
(a)	57855.105	3.5×2.7	70.1	7.0 ± 1.1	...	18.9	$+10.290 \pm 0.085$	$+8.770 \pm 0.082$
(b)	57924.915	3.6×2.7	72.8	3.2 ± 0.6	...	8.9	$+2.845 \pm 0.173$	$+0.332 \pm 0.157$
(c)	58015.664	4.7×3.4	81.0	3.2 ± 0.7	...	6.4	$+0.453 \pm 0.351$	-11.573 ± 0.263
(d)	58107.134	4.8×1.0	5.4	...	4.1 ± 0.8	8.6	$+13.865 \pm 0.076$	-26.277 ± 0.261
(e)	58249.725	5.0×1.0	11.6	...	6.5 ± 1.2	8.8	$+17.022 \pm 0.074$	-45.928 ± 0.186
(f)	58374.439	5.7×1.2	9.1	...	9.4 ± 2.0	6.5	$+9.523 \pm 0.097$	-62.039 ± 0.327

Note. ^aCol. 1: Panel code in Fig. 2, Col. 2: Modified Julian Day (MJD), Col. 3: size of the synthesized beam, Col. 4: position angle, Cols 5 and 6: peak brightness at 5 GHz or 8.6 GHz, Col. 7: signal-to-noise ratio (SNR) of images, and Cols 8 and 9: relative position offset.

S/X-band coordinate of $\alpha_{J2000} = 16^{\text{h}}25^{\text{m}}46^{\text{s}}.8916429 \pm 0.03$ mas, $\delta_{J2000} = -25^{\circ}27'38''.326873 \pm 0.03$ mas. Finally, we provided the position of J1621–2241 of $\alpha_{J2000} = 16^{\text{h}}21^{\text{m}}32^{\text{s}}.27524 \pm 1.0$ mas, $\delta_{J2000} = -22^{\circ}41'01''.3982 \pm 1.7$ mas, with the uncertainty given by the combination of the uncertainty in the weighted mean position of J1621–2241 and the uncertainty in the ICRF3 position of J1625–2527.

With respect to J1621–2241, we measured the astrometric parameters at the epoch J2018 for AR Sco. The AIPS task JMFIT was used to derive the radio centroid of AR Sco at each epoch. The final position offsets and the formal position uncertainties are listed in Table 3. These formal position uncertainties are the combinations of the statistical error extracted in the image by the AIPS task JMFIT and the astrometric error caused by the phase-referencing technology. For the latter, we derived an estimate of 0.07 mas from Pradel,

Charlot & Lestrade (2006) based on the position offset between the target and the secondary calibrator. For the astrometric fit, the effect caused by the potential core shift in the secondary calibrator was considered. No obvious jet structure was detected for the secondary calibrator in our observations. The typical frequency-dependent core shift of 0.11 mas in each direction between 5 GHz and ~ 8.6 GHz (Sokolovsky et al. 2011) was added as a term of systemic error to the position uncertainties which were derived from EVN observations for AR Sco.

A bootstrap approach (e.g. Efron & Tibshirani 1991; Deller et al. 2019) for astrometric fit was performed on the position offsets and their uncertainties for AR Sco. We conducted 10 000 times random sampling with replacement from the available six data points. A least-squares fit was performed for each sampled data set. At last, a statistical distribution was obtained for each parameter. Fig. 3

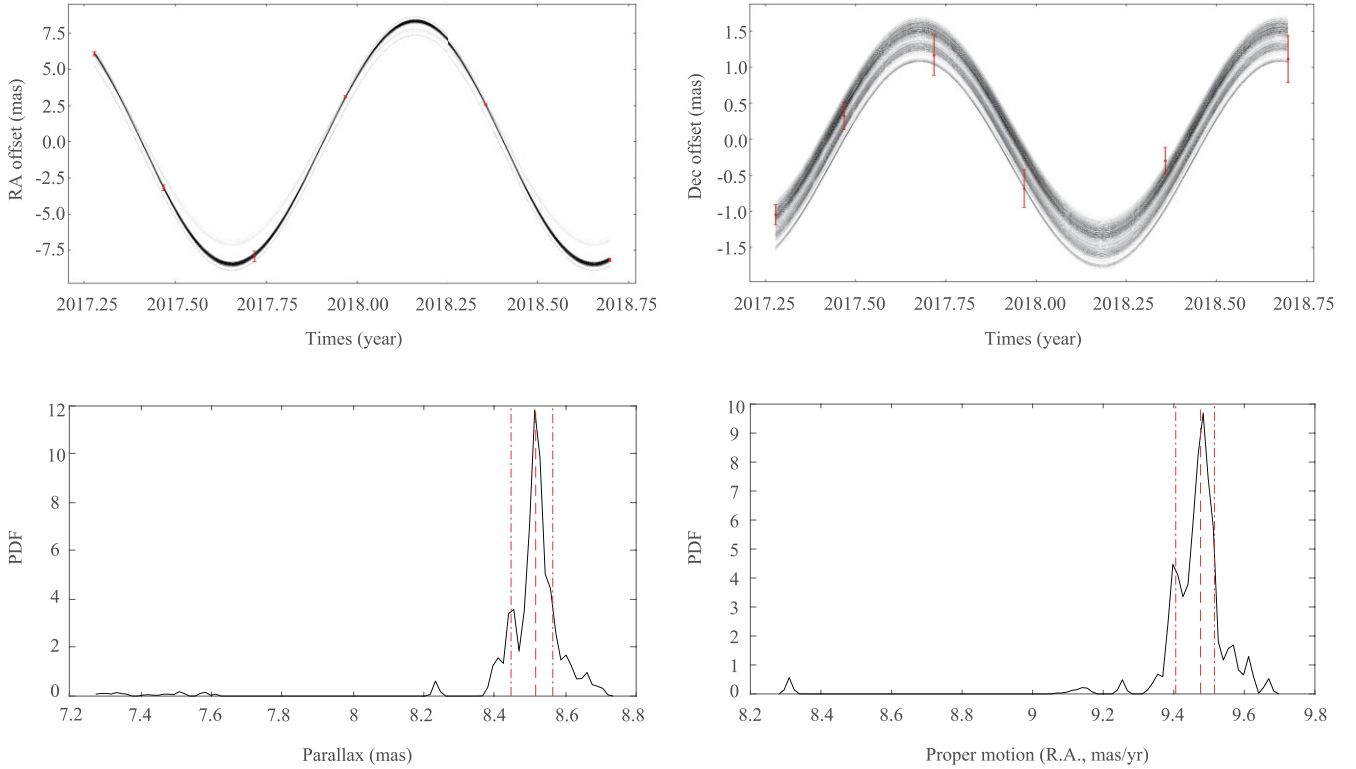


Figure 3. Top: Illustration of the bootstrap astrometric fit for AR Sco, showing position offset in right ascension (left) and declination (right) with the proper motion removed. Each of the 10 000 trial fits is plotted in light grey line. Bottom: probability distribution functions (PDF) of parallax (left) and proper motion in right ascension (right). The median values and the 68 percent confidence intervals are indicated with red vertical dashed lines and red vertical dot-dashed lines, respectively.

Table 4. Fitted astrometric parameters for AR Sco at epoch J2018.

Parameter	This work (w.r.t ICRF3)	This work (w.r.t <i>Gaia</i> -CRF)	<i>Gaia</i> Collaboration 2021
α_0 (h m s)	16 21 47.29576 $^{+0.00007}_{-0.00007}$	16 21 47.295729 $^{+0.000070}_{-0.000070}$	16 21 47.295820 $^{+0.0000072}_{-0.0000072}$
δ_0 ($^{\circ}$ $'$ $''$)	-22 53 11.3164 $^{+0.0018}_{-0.0018}$	-22 53 11.31303 $^{+0.00072}_{-0.00075}$	-22 53 11.31249 $^{+0.000080}_{-0.000080}$
μ_α (mas yr $^{-1}$)	9.48 $^{+0.04}_{-0.07}$	9.48 $^{+0.04}_{-0.07}$	9.690 $^{+0.047}_{-0.047}$
μ_δ (mas yr $^{-1}$)	-51.32 $^{+0.22}_{-0.38}$	-51.32 $^{+0.22}_{-0.38}$	-51.489 $^{+0.038}_{-0.038}$
π (mas) ^a	8.52 $^{+0.04}_{-0.07}$	8.52 $^{+0.04}_{-0.07}$	8.586 $^{+0.040}_{-0.040}$

Note. ^aA zero-point correction has been applied to the *Gaia* parallax.

shows the bootstrap astrometric fit and bootstrap histograms for AR Sco. According to the median value and the statistical 68 per cent confidence interval, we derived a parallax of $\pi = 8.52^{+0.04}_{-0.07}$ mas. The other astrometric parameters were also derived in the same way and the results are listed in Table 4. Note that we used both the *Gaia* EDR3 position and our VLBI position of J1621–2241 to calculate the position of AR Sco, so each result is with respect to the celestial reference frame of *Gaia* (*Gaia*-CRF; *Gaia* Collaboration 2022) and ICRF3, respectively. The position uncertainties of J1621–2241 were taken into account for estimating the position uncertainties of AR Sco. For the *Gaia* EDR3 position of J1621–2241, a median radio-optical positional offset of 0.5 mas from *Gaia* Collaboration (2022) was added to the position uncertainties.

The reduced chi-squared of the least-squares fit was performed to verify the bootstrap astrometric fit. The illustration of the final

astrometric fit is shown in Fig. 4. We obtained a parallax estimate of $\pi = 8.53 \pm 0.07$ mas and proper motion estimates of $\mu_\alpha = 9.47 \pm 0.09$ mas yr $^{-1}$, $\mu_\delta = -51.37 \pm 0.19$ mas yr $^{-1}$ for AR Sco. All astrometric parameters derived by the reduced chi-squared method are well consistent with those extracted from the bootstrap approach. Therefore, the reduced chi-squared astrometric fit validates the bootstrap results. We report the bootstrap results as our final results.

4 DISCUSSION

4.1 Comparison with results of *Gaia* EDR3

We obtained independent astrometric measurements for AR Sco at the radio band in Section 3. In optical, *Gaia* EDR3 provided astrometric results for AR Sco as listed in Table 4. The *Gaia* position was calculated to epoch J2018 and a direct comparison

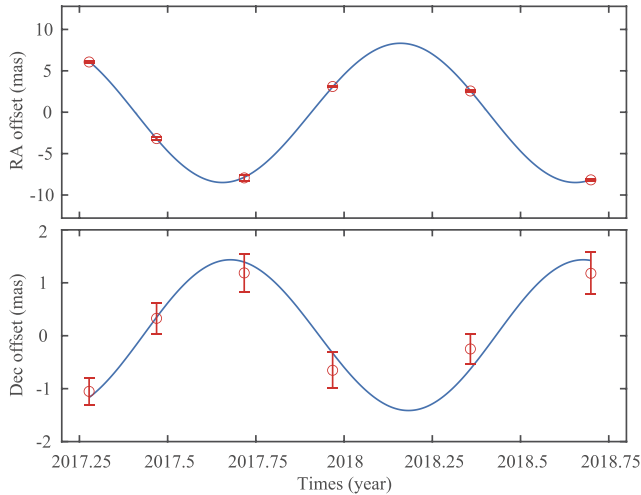


Figure 4. The least-squares astrometric fit for AR Sco, showing position offset in right ascension (upper) and declination (bottom) with the proper motion removed.

with our VLBI results can be performed. The position parameters for the VLBI results were derived in both ICRF3 and *Gaia*-CRF. The differences between the VLBI positions and the *Gaia*'s are smaller than or close to 1σ uncertainties in *Gaia*-CRF. In ICRF3, the difference in position in RA is smaller than 1σ uncertainty and the difference in position in Dec. is quite close to 2σ uncertainty. We note that the uncertainties in the position of AR Sco are dominated by those of its reference source J1621–2241. Future astrometric VLBI observations for J1621–2241 will give improved estimates in the position of AR Sco. At present, there is no obvious offset between the optical and radio positions of AR Sco.

For the *Gaia* parallax, a zero-point correction of -0.043 mas from Lindegren et al. (2021) and an inflated error bar of 0.040 mas from El-Badry, Rix & Heintz (2021) has been applied to the raw *Gaia* parallax $\pi = 8.544 \pm 0.038$ mas. We found that the VLBI parallax was consistent with the raw *Gaia* parallax within 1σ . However, the difference between the VLBI parallax and the zero-point corrected *Gaia* parallax slightly exceeds 1σ . The global parallax bias for *Gaia* EDR3 measured from a large number of quasars is $17 \mu\text{as}$ (Lindegren et al. 2021). Compared with the global parallax bias, the value of the zero-point correction of -0.043 mas for AR Sco is relatively large. AR Sco is situated at small Galactic latitude ($\sim 19^\circ$) could explain it, in which a small number of quasars identified and a possible contamination of the quasars sample caused by Galactic stars leads to the difficulty of estimates of zero-point corrections. In addition, the zero-point estimates are well populated by the quasars at magnitude $G \geq 16$. Beyond that region, the uncertainties of the zero-point corrections will be greater (Lindegren et al. 2021). The apparent magnitude of AR Sco in the *Gaia* G band is 14.99, beyond that region. VLBI astrometric observations of radio stars can validate the quality of *Gaia*-CRF and help to determine the parallax zero-point of *Gaia* catalogue (e.g. Bobylev 2019; Xu et al. 2019; Lindegren 2020). Our high-precision VLBI results for AR Sco can be used as independent measurements for the aims.

In a word, the VLBI results are consistent with the *Gaia* result with no obvious offset. Here, we derived astrometric parameters for AR Sco with the combination of VLBI and *Gaia* result. The weighted average method was used to derive new astrometric parameter. The weights of astrometric parameters were set to be inversely proportional to the square of their uncertainties during the

calculation. We obtain the parallax ($\pi = 8.57 \pm 0.03$ mas), and proper motion ($\mu_\alpha = 9.62 \pm 0.04$ mas yr $^{-1}$, $\mu_\delta = -51.49 \pm 0.04$ mas yr $^{-1}$), for AR Sco.

4.2 Kinematics

We computed the Galactic space velocities U , V , and W for AR Sco in a right-handed system following Johnson & Soderblom (1987) where U , V , and W were measured positive in the directions of the Galactic Centre, the Galactic rotation, and the North Galactic Pole, respectively. An assumption of zero radial velocity for the target AR Sco was adopted to calculate the Galactic space velocities (e.g. Sion et al. 2014). A motion of the Sun of $(U_\odot, V_\odot, W_\odot) = (10.1, 13.6, 7.0)$ km s $^{-1}$ (Bobylev et al. 2021) relative to the local standard of rest was adopted for the solar motion correction. By using the astrometric results obtained in Section 4.1, we derived Galactic space velocities of $(U, V, W) = (15.4, -4.8, -14.7)$ km s $^{-1}$, corresponding to a total velocity of $T = 21.8$ km s $^{-1}$, for AR Sco.

For AR Sco, its non-synchronous spin and orbital periods imply a connection with IPs. Takata et al. (2018) categorized AR Sco as an unusual IP directly. However, the lack of Doppler-broadened line emission is indicative of the absence of accretion discs, and the weak X-ray radiation implies that the majority of its luminosity is not attributable to accretion. In contrast, accretion is the main power source for most IPs (e.g. Buckley 2000). A more reliable hypothesis is that AR Sco represents an evolutionary stage of IPs (Marsh et al. 2016). In this sense, AR Sco could be a progenitor star of IPs (Meintjes 2018) or a transitional star lying between IPs and traditional polars (Katz 2017). Moreover, Schreiber et al. (2021) presented evolutionary models for the magnetic WDs in close binary stars and suggested that AR Sco is a progenitor star of polars. AR Sco represents a short spin-down phase for strongly magnetic WDs in binaries in their evolutionary sequence. The stage occurs at the beginning of synchronization of the spin and orbital period for strongly magnetic WD binaries and finally polars will be formed.

Here, we investigate the kinematics of AR Sco relative to a sample of 82 IPs and 107 polars. The kinematics and statistics of IPs and polars can be seen in Appendix A. Statistics show that IPs have significantly lower velocity dispersion than IP candidates. Polars have slightly lower velocity dispersion than polar candidates. The kinematic properties of IPs and polars are highly similar to each other, as both IPs and polars are sub-type stars of magnetic cataclysmic variables. In Fig. 5, we plotted $U - V$ space velocity diagram for the sample and AR Sco. Being an unique source, AR Sco, however, is not an outlier with respect to both IPs and polars as shown in Fig. 5. Its Galactic space velocities are quite consistent with that of both IPs and polars. This is reasonable under the assumptions that AR Sco now goes through a short-lived spin-down evolutionary stage of IPs or polars.

4.3 Radio emitting region

The parallax derived from the combinations of VLBI and *Gaia* results sets AR Sco at a distance of 116.7 ± 0.4 pc. With a source size of 0.17 mas of AR Sco obtained with the LBA at 8.4 GHz reported by Marcote et al. (2017), the distance establishes that the radio emitting region size is $\lesssim 3 \times 10^{11}$ cm. The size is only about half the light cylinder radius ($R_{LC} \sim 6 \times 10^{11}$ cm) of the WD. This implies that the main radio emission region is situated inside the light cylinder of the WD. The finding is in agreement with what Singh et al. (2020) derived from γ -ray data and favours the models in which the main radio emission comes from a region near the WD, or the M star as

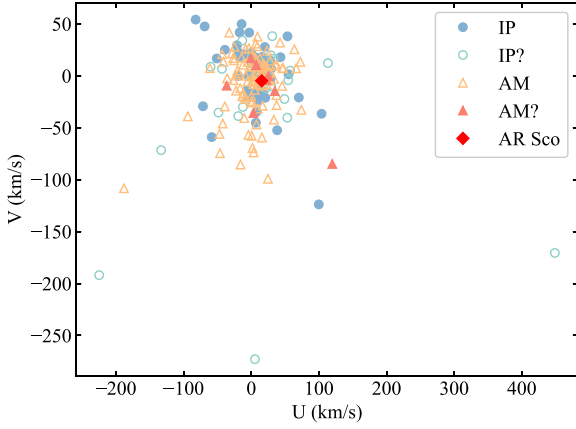


Figure 5. $U - V$ space velocity diagram for AR Sco and the sample of IPs and polars.

this companion is situated well inside the magnetosphere of the WD (e.g. Geng et al. 2016; Katz 2017).

4.4 Orbital reflex motion

For AR Sco, the mass of the WD and M star were derived as $M_{\text{WD}} \approx 0.8 M_{\odot}$ and $M_{\text{M}} \approx 0.3 M_{\odot}$, respectively (Marsh et al. 2016). With the measured orbital period $P = 0.14853528(8)$ d and circular orbit, the orbital radius of the WD is $R_{\text{WD}} \sim 2 \times 10^{10}$ cm, and the orbital radius of the secondary star is $R_{\text{M}} \sim 6 \times 10^{10}$ cm. Based on the distance of AR Sco, an amplitude of possible reflex motion of $\sim 40 \mu\text{as}$ could be expected under the assumption that the non-thermal emission originates from the MD’s atmosphere (e.g. Katz 2017). For those scenarios in which the radio emission region close to the MD surface (e.g. du Plessis et al. 2022), a smaller amplitude of $\sim 10 \mu\text{as}$ may occur. In any case, the amplitude is below the measurement accuracy for our observations. The effect caused by the orbital motion is negligible based on the positions of AR Sco were derived with integral time close to or longer than the orbital period in our measurements. Additionally, the calculations imply that the possible detection of the orbital reflex motion for the non-thermal emission could help to constrain the emitting region location for AR Sco. The microarcsecond VLBI astrometry with high sensitivity will make an effort in the future. For instance, the $\sim 10 \mu\text{as}$ goal of astrometry using VLBI with the Square Kilometer Array was suggested to be feasible by using the MultiView technique (Rioja et al. 2017).

4.5 Revisiting other physical parameters

Based on the M star’s spectra and brightness, Marsh et al. (2016) derived a distance estimate $d \approx 116 [M_{\text{M}} / (0.3 M_{\odot})]^{1/3}$ pc for AR Sco, assuming that the M star was close to its Roche lobe and its mass $M_{\text{M}} \approx 0.3 M_{\odot}$. Adopting the distance of 116 pc to the spectral energy distribution of this system, they obtained a maximum luminosity of $L_{\text{max}} \approx 6.3 \times 10^{25}$ W. They also measured the orbital period $P = 0.14853528(8)$ d and the radial velocity amplitude of the M star $K = 295 \pm 4 \text{ km s}^{-1}$, and defined the mass function

$$\frac{M_{\text{WD}}^3 \sin^3 i}{(M_{\text{WD}} + M_{\text{M}})^2} = \frac{PK^3}{2\pi G} = (0.395 \pm 0.016) M_{\odot}, \quad (1)$$

where i is the orbital inclination.

Our measurements obtained a more accurate distance for AR Sco. A mass of $M_{\text{M}} \approx 0.31 M_{\odot}$ for the M star was derived from the distance–mass relation $d \approx 116 [M_{\text{M}} / (0.3 M_{\odot})]^{1/3}$ with our distance. Following the assumption suggested by du Plessis et al. (2019) that the orbital inclination i is approximately equal to the observer angle $\zeta = 60.4_{-6.0}^{+5.3}$, we solve the mass function (1) with $M_{\text{M}} \approx 0.31 M_{\odot}$, and derived $M_{\text{WD}} \approx 1.0_{-0.1}^{+0.2} M_{\odot}$ for the WD. However, the observer angle provided by du Plessis et al. (2019) was derived from polarization position angle data which were averaged over a large range of orbital phase. An updated work performed by du Plessis et al. (2022) shows a variation of $\sim 30^\circ$ in ζ over the orbital period, the ζ is approximately in range from 55° to 85° . Based on these results, we provide a more conservative estimate of $M_{\text{WD}} \approx 1.0 \pm 0.2 M_{\odot}$ for the WD. Our distance also resets the maximum luminosity of $L_{\text{max}} \approx 6.4 \times 10^{25}$ W for AR Sco.

Our parallax supports the distance estimated by Marsh et al. (2016), and the recalculation shows that no substantial correction is needed to these physical parameters of AR Sco.

5 SUMMARY

With the EVN observations at 5 GHz and the CVN plus Wa observations at 8.6 GHz, we clearly detected the compact radio emission of the only-known WD pulsar AR Sco in the epochs between 2017 February and 2018 September. Using a nearby calibrator, 12 arcmin apart from AR Sco, we provide high-precision measurements on the parallax ($\pi = 8.52_{-0.07}^{+0.04}$ mas), and proper motion ($\mu_{\alpha} = 9.48_{-0.07}^{+0.04}$ mas yr $^{-1}$, $\mu_{\delta} = -51.32_{-0.38}^{+0.22}$ mas yr $^{-1}$), for AR Sco. The independent measurements are consistent with the *Gaia* EDR3 reports. Kinematic analysis shows that the Galactic space velocities of AR Sco are quite consistent with that of intermediate polars and polars. Together with the early tightest VLBI constraint on the size, our parallax distance suggests that the radio emission of AR Sco would be located within the light cylinder of its WD. Furthermore, we revisit the mass and luminosity of AR Sco with the parallax distance and confirm the previous estimates reported by Marsh et al. (2016).

ACKNOWLEDGEMENTS

We thank Sandor Frey, Kazuhiro Hada, and the anonymous referee for helpful discussions and constructive suggestions, which resulted in an overall improvement of the paper. This work is supported by the CAS ‘Light of West China’ Program (grant no. 2021-XBQNXX-005) and the National Natural Science Foundation of China (grant nos. U2031212, 11673051, and U1831136). LC is also thankful for the support of the Youth Innovation Promotion Association of the CAS (No. 2017084). The European VLBI Network is a joint facility of independent European, African, Asian, and North American radio astronomy institutes. Scientific results from data presented in this publication are derived from the following EVN project codes: RSC03 and EL058. e-VLBI research infrastructure in Europe is supported by the European Union’s Seventh Framework Programme (FP7/2007-2013) under grant agreement number RI-261525 NEXPREs. We are thankful for the observation time of the Chinese VLBI Network and the Warkworth 30-m radio telescope operated by the Institute for Radio Astronomy and Space Research, Auckland University of Technology. The computing cluster of Shanghai VLBI correlator supported by the Special Fund for Astronomy from the Ministry of Finance in China is acknowledged. This work has made use of data from the European Space Agency

(ESA) mission *Gaia* (<https://www.cosmos.esa.int/gaia>), processed by the *Gaia* Data Processing and Analysis Consortium (DPAC, <https://www.cosmos.esa.int/web/gaia/dpac/consortium>). Funding for the DPAC has been provided by national institutions, in particular the institutions participating in the *Gaia* Multilateral Agreement. This research has made use of the SIMBAD data base, operated at CDS, Strasbourg, France.

DATA AVAILABILITY

The correlated data of the experiments RSC03 and EL058 are available in the EVN data archive (<http://archive.jive.nl/scripts/portals.php>). The correlated data of the experiments CC001 can be requested from the corresponding author. The *Gaia* EDR3 data underlying this article are available in the *Gaia* Archive (<https://gea.esac.esa.int/archive/>). The ICRF3 catalogue is available at the website of the International Earth Rotation and Reference Systems Service (<https://hpiers.obspm.fr/icrs-pc/newwww/index.php>).

REFERENCES

- Bednarek W., 2018, *MNRAS*, 476, L10
 Bobylev V. V., 2019, *Astron. Lett.*, 45, 10
 Bobylev V. V., Bajkova A. T., Rastorguev A. S., Zabolotskikh M. V., 2021, *MNRAS*, 502, 4377
 Bookbinder J. A., Lamb D. Q., 1987, *ApJ*, 323, L131
 Buckley D. A. H., 2000, *New Astron. Rev.*, 44, 63
 Buckley D. A. H., Meintjes P. J., Potter S. B., Marsh T. R., Gänsicke B. T., 2017, *Nat. Astron.*, 1, 0029
 Charlot P. et al., 2020, *A&A*, 644, A159
 Deller A. T. et al., 2011, *PASP*, 123, 275
 Deller A. T. et al., 2019, *ApJ*, 875, 100
 Doi A. et al., 2006, *PASJ*, 58, 777
 du Plessis L., Wadiasingh Z., Venter C., Harding A. K., 2019, *ApJ*, 887, 44
 du Plessis L., Venter C., Wadiasingh Z., Harding A. K., Buckley D. A. H., Potter S. B., Meintjes P. J., 2022, *MNRAS*, 510, 2998
 Efron B., Tibshirani R., 1991, *Science*, 253, 390
 El-Badry K., Rix H.-W., Heintz T. M., 2021, *MNRAS*, 506, 2269
 Fey A. L., Clegg A. W., Fomalont E. B., 1996, *ApJS*, 105, 299
 Franzon B., Schramm S., 2017, *MNRAS*, 467, 4484
 Gaia Collaboration, 2016, *A&A*, 595, A2
 Gaia Collaboration, 2021, *A&A*, 649, A1
 Gaia Collaboration, 2022, *A&A*, 667, A148
 Garnavich P., Littlefield C., Kafka S., Kennedy M., Callanan P., Balsara D. S., Lyutikov M., 2019, *ApJ*, 872, 67
 Geng J.-J., Zhang B., Huang Y.-F., 2016, *ApJ*, 831, L10
 Greisen E. W., 2003, in Heck A., ed., *Astrophysics and Space Science Library* Vol. 285, Information Handling in Astronomy - Historical Vistas. Springer-Verlag, Berlin, p. 109
 Griffith M. R., Wright A. E., Burke B. F., Ekers R. D., 1994, *ApJS*, 90, 179
 Halpern J. P., Thorstensen J. R., 2022, *ApJ*, 924, 67
 Hilton E. J., Szkody P., Mukadam A., Henden A., Dillon W., Schmidt G. D., 2009, *AJ*, 137, 3606
 Johnson D. R. H., Soderblom D. R., 1987, *AJ*, 93, 864
 Katz J. I., 2017, *ApJ*, 835, 150
 Keimpema A. et al., 2015, *Exp. Astron.*, 39, 259
 Kubiak M., Krzeminski W., 1994, *Acta Astron.*, 44, 81
 Lindegren L., 2020, *A&A*, 633, A1
 Lindegren L. et al., 2021, *A&A*, 649, A4
 Marcote B., Marsh T. R., Stanway E. R., Paragi Z., Blanchard J. M., 2017, *A&A*, 601, L7
 Marsh T. R. et al., 2016, *Nature*, 537, 374
 Meintjes P., 2018, *PoS, MULTIF2017*, 44
 Oruru B., Meintjes P. J., 2012, *MNRAS*, 421, 1557
 Papadaki C., Boffin H. M. J., Sterken C., Stanishev V., Cuypers J., Boumiev P., Akras S., Alikakos J., 2006, *A&A*, 456, 599
 Paragi Z. et al., 2013, *MNRAS*, 432, 1319
 Patterson J., 1994, *PASP*, 106, 209
 Pradel N., Charlot P., Lestrade J. F., 2006, *A&A*, 452, 1099
 Rioja M. J., Dodson R., Orosz G., Imai H., Frey S., 2017, *AJ*, 153, 105
 Ritter H., Kolb U., 2003, *A&A*, 404, 301
 Rosen S. R., Watson T. K., Robinson E. L., Prinja R. K., Misselt K., Shafter A. W., 1995, *A&A*, 300, 392
 Sambruna R. M. et al., 1992, *ApJ*, 391, 750
 Schreiber M. R., Belloni D., Gänsicke B. T., Parsons S. G., Zorotovic M., 2021, *Nat. Astron.*, 5, 648
 Shepherd M. C., Pearson T. J., Taylor G. B., 1994, *BAAS*, 26, 987
 Singh K. K., Meintjes P. J., Kaplan Q., Ramamonjisoa F. A., Sahayanathan S., 2020, *Astropart. Phys.*, 123, 102488
 Sion E. M., Holberg J. B., Oswalt T. D., McCook G. P., Wasatonic R., Myszkaj J., 2014, *AJ*, 147, 129
 Sokolovsky K. V., Kovalev Y. Y., Pushkarev A. B., Lobanov A. P., 2011, *A&A*, 532, A38
 Szomoru A., 2009, *PoS, IX EVN Symposium*, 40
 Takata J., Hu C. P., Lin L. C. C., Tam P. H. T., Pal P. S., Hui C. Y., Kong A. K. H., Cheng K. S., 2018, *ApJ*, 853, 106
 Wenger M. et al., 2000, *A&AS*, 143, 9
 Woodburn L., Natusch T., Weston S., Thomasson P., Godwin M., Granet C., Gulyaev S., 2015, *Publ. Astron. Soc. Aust.*, 32, e017
 Worpel H., Schwöpe A. D., Traulsen I., Mukai K., Ok S., 2020, *A&A*, 639, A17
 Xu S., Zhang B., Reid M. J., Zheng X., Wang G., 2019, *ApJ*, 875, 114
 Yakin D. G., Suleimanov V. F., Vlasyuk V. V., Spiridonova O. I., 2013, *Astron. Lett.*, 39, 38
 Yang J., Gurvits L. I., Paragi Z., Frey S., Conway J. E., Liu X., Cui L., 2020, *MNRAS*, 495, L71
 Zacharias N., Finch C., Frouard J., 2017, *AJ*, 153, 166
 Zemko P. et al., 2018, *MNRAS*, 480, 4489

APPENDIX A: KINEMATICS AND STATISTICS OF IPS AND POLARS

Table A1 presents a sample of IPs and polars with Galactic space motion results. We assembled this sample by starting with a traversal search on the *Catalogue of Cataclysmic Binaries, Low-Mass X-Ray Binaries and Related Objects* (Edition 7.24, Ritter & Kolb 2003). We obtained a sample of 280 stars for IPs and polars and found that 189 stars already had *Gaia* EDR3 results (the position, the parallax and the proper motion) be identified in the SIMBAD astronomical data base (Wenger et al. 2000). The sample of 189 stars consists of 82 IPs and 107 polars. The Galactic space velocity calculations for this sample followed the same method described in Section 4.2. The resultant space motion parameters are listed in Table A1 and the corresponding statistical information is listed in Table A2.

Table A1. Kinematics for the sample of IPs and polars.

Name	Type ^a	<i>U</i>	<i>V</i>	<i>W</i>	<i>T</i>	Name	Type ^a	<i>U</i>	<i>V</i>	<i>W</i>	<i>T</i>
GK Per	IP	11.4	2.4	-29.7	31.9	J1740 – 2847	IP	10.0	-0.4	4.6	11.0
V2731 Oph	IP	-3.0	41.6	21.5	46.9	EX Hya	IP	-19.4	-0.2	13.9	23.9
V1062 Tau	IP	13.8	11.6	-13.6	22.5	DW Cnc	IP	-2.0	18.7	-14.5	23.8
NY Lup	IP	-4.2	-21.1	-20.1	29.4	HT Cam	IP	8.1	9.6	7.0	14.3
V902 Mon	IP	19.8	-1.3	-10.3	22.3	FS Aur	IP	10.6	-23.7	34.1	42.8
J0838 – 4831	IP	-51.0	16.7	14.3	55.6	V1025 Cen	IP	-71.4	-29.3	15.5	78.8
V2069 Cyg	IP	26.8	12.7	6.6	30.4	CC Scl	IP	70.3	-20.9	25.4	77.6
J0457 + 4527	IP	11.0	17.1	-4.9	20.9	J0503 – 2823	IP	-69.0	47.6	42.6	94.0
J2133 + 5107	IP	27.5	15.0	10.3	33.0	J0525 + 2413	IP	10.4	-1.2	7.9	13.1
El UMa	IP	-1.5	-0.5	-5.1	5.3	J0614 + 1704	IP	17.1	-15.2	1.4	22.9
J1509 – 6649	IP	-4.2	0.1	0.0	4.2	J2015 + 3711	IP	55.1	1.4	9.2	55.9
V3037 Oph	IP	9.8	-10.9	8.0	16.7	AE Aqr	IP	-11.1	20.7	-14.7	27.7
WX Pyx	IP	-19.7	22.7	-16.9	34.5	DQ Her	IP	-17.8	18.1	14.6	29.3
TV Col	IP	-39.0	25.0	36.3	58.9	V349 Aqr	¹ IP	99.9	-123.8	-81.7	178.8
V709 Cas	IP	9.4	12.5	-2.8	15.9	V598 Peg	² IP	43.2	17.9	7.5	47.4
PQ Gem	IP	-14.3	49.8	-9.7	52.7	J1832 – 0840	³ IP	38.2	-52.4	-1.6	64.9
HZ Pup	IP	-82.3	54.1	-3.3	98.5	QR And	IP?	-224.9	-192.0	-105.9	314.1
FO Aqr	IP	0.3	22.2	7.8	23.5	J0939 – 3226	IP?	-60.2	8.7	-45.3	75.8
MU Cam	IP	16.0	18.2	10.8	26.5	V2275 Cyg	IP?	113.3	12.2	13.2	114.7
HY Leo	IP	20.8	-21.2	-7.4	30.6	V426 Oph	IP?	29.4	-10.0	-7.6	31.9
V1323 Her	IP	103.9	-36.6	26.1	113.2	V1039 Cen	IP?	-48.5	-35.4	9.3	60.8
V418 Gem	IP	6.2	11.3	-9.8	16.2	AH Eri	IP?	53.2	-40.3	-8.3	67.3
V2306 Cyg	IP	29.3	6.9	-13.3	32.9	AP Cru	IP?	-133.3	-71.6	3.7	151.3
LS Peg	IP	1.0	-1.1	-22.3	22.4	J1616 – 4958	IP?	6.5	6.5	4.3	10.2
V405 Aur	IP	-6.1	-14.0	-14.0	20.7	V4745 Sgr	IP?	5.5	-272.9	-48.0	277.1
V1033 Cas	IP	53.5	38.0	-4.7	65.8	GI Mon	IP?	-13.3	34.0	-31.5	48.3
J1719 – 4100	IP	7.0	-1.1	13.8	15.5	CW Mon	IP?	17.8	-0.7	21.0	27.5
DO Dra	IP	20.1	27.7	2.6	34.3	J1446 + 0253	IP?	49.1	-22.4	-23.6	58.8
J0153 + 7446	IP	10.5	12.5	12.2	20.4	V2467 Cyg	IP?	57.5	4.9	18.2	60.5
V842 Cen	IP	-58.5	-59.0	4.9	83.3	LS Cam	IP?	31.0	38.2	9.0	50.0
J1654 – 1916	IP	7.7	-34.8	20.8	41.2	V592 Cas	IP?	28.9	19.8	-22.7	41.7
J1649 – 3307	IP	4.7	-18.3	3.7	19.3	GZ Cnc	IP?	-12.4	-30.0	-55.9	64.6
AO Psc	IP	10.4	-23.1	-18.3	31.2	VZ Pyx	IP?	0.6	12.0	-12.1	17.1
V647 Aur	IP	13.6	-1.2	23.5	27.1	BZ UMa	IP?	19.6	1.4	23.4	30.6
UU Col	IP	-21.3	29.4	13.9	38.8	YY Sex	IP?	21.3	-12.2	-14.7	28.6
J1926 + 1322	IP	28.5	-2.8	-1.9	28.7	QZ Vir	IP?	-19.3	-38.8	-24.3	49.7
J2014 + 1529	IP	21.8	6.2	8.6	24.3	V533 Her	IP?	0.6	17.7	6.0	18.7
V2400 Oph	IP	8.6	17.3	16.8	25.6	KO Vel	^{4,5} IP?	-43.4	6.7	10.8	45.2
V1223 Sgr	IP	6.8	-45.2	-25.7	52.5	J2216 + 4646	⁶ IP?	33.6	16.4	5.3	37.7
BG CMi	IP	-17.2	41.8	-37.5	58.7	V795 Her	^{7,8} IP?	54.6	-4.3	-7.0	55.2
V515 And	IP	16.7	11.1	-12.2	23.5	V2491 Cyg	⁹ IP?	449.0	-170.5	5.9	480.3
V479 And	AM	63.7	25.5	-16.6	70.6	EK UMa	AM	-46.3	-74.6	-1.2	87.8
V1309 Ori	AM	16.6	-9.6	12.3	22.8	ST LMi	AM	17.7	-4.1	5.7	19.0
AI Tri	AM	22.7	-8.1	-33.1	40.9	BL Hyi	AM	-18.6	2.4	4.8	19.4
J0649-0737	AM	20.4	1.3	5.5	21.1	MR Ser	AM	-28.6	21.6	33.1	48.8
MQ Dra	AM	1.8	-5.8	25.6	26.3	FR Lyn	AM	1.8	-69.5	-8.5	70.1
J2048 + 0050	AM	5.8	17.6	7.3	19.9	V884 Her	AM	-8.5	26.0	20.9	34.4
V1043 Cen	AM	3.1	-8.1	-15.3	17.6	V2301 Oph	AM	-3.6	26.6	21.7	34.5
0922 + 1333	AM	14.1	-2.0	-0.7	14.2	CD Ind	AM	-16.4	-12.0	-9.4	22.4
VY For	AM	0.0	-19.9	28.2	34.5	J1002 – 1925	AM	-25.3	14.9	-5.6	29.9
J0227 + 1306	AM	36.2	9.4	-20.0	42.4	EP Dra	AM	-61.2	7.3	-7.3	62.0
QQ Vul	AM	27.8	3.3	-0.3	28.0	J0953 + 1458	AM	42.5	31.9	41.3	67.3
J0749-0549	AM	20.7	-3.3	-17.9	27.5	J0706 + 0324	AM	37.4	-28.2	22.3	51.9
V358 Aqr	AM	5.1	-13.6	-9.7	17.4	V834 Cen	AM	-22.5	-14.3	24.3	36.0
J1007-2017	AM	-12.1	10.7	-6.4	17.4	VV Pup	AM	45.6	-9.8	-7.8	47.3
V388 Peg	AM	37.2	-18.7	-21.1	46.6	EG Lyn	AM	0.7	-57.8	12.2	59.1
J1422-0221	AM	19.5	8.6	-0.8	21.3	J1344 + 2044	AM	24.6	-99.2	7.4	102.5
V1432 Aql	AM	16.9	10.2	22.7	30.1	V393 Pav	AM	-9.9	-20.6	-4.5	23.3
BY Cam	AM	9.1	37.6	-36.5	53.2	HS Cam	AM	2.3	-3.9	10.9	11.8
V1500 Cyg	AM	72.6	13.4	13.5	75.1	LW Cam	AM	18.5	11.5	24.9	33.1
J0733 + 2619	AM	11.6	1.4	3.5	12.2	BS Tri	AM	11.0	-8.1	-15.6	20.7
J0837 + 3830	AM	-13.1	-19.6	-27.0	35.9	EQ Cet	AM	-4.2	-56.9	11.7	58.2
V519 Ser	AM	22.1	9.3	-6.7	24.9	J1944 – 4202	AM	6.6	31.0	-1.3	31.7
J1453-5521	AM	-47.0	-56.0	-15.8	74.8	J1312 + 1736	AM	23.4	24.2	5.8	34.2
CW Hyi	AM	-39.2	-29.5	29.7	57.3	J1321 + 5609	AM	46.9	7.6	18.7	51.1

Table A1 – continued

Name	Type ^a	<i>U</i>	<i>V</i>	<i>W</i>	<i>T</i>	Name	Type ^a	<i>U</i>	<i>V</i>	<i>W</i>	<i>T</i>
J2319 + 2615	AM	14.7	5.2	-7.3	17.2	EU UMa	AM	-5.7	-5.6	1.7	8.2
HY Eri	AM	33.4	-42.2	8.7	54.5	V347 Pav	AM	2.9	18.2	-10.6	21.2
WX LMi	AM	20.5	-3.3	13.1	24.5	J0257 + 3337	AM	7.8	2.0	-1.7	8.2
EU Lyn	AM	6.0	13.3	-1.0	14.6	J0502 + 1624	AM	9.8	-31.7	22.9	40.3
V349 Pav	AM	8.8	28.4	-6.2	30.4	DP Leo	AM	-26.4	-4.2	-9.0	28.2
PZ Vir	AM	-35.7	-2.5	19.4	40.7	CP Tuc	AM	0.8	-24.3	17.9	30.2
J0524 + 4244	AM	-0.5	-25.8	-4.2	26.2	J1514 + 0744	AM	3.3	-73.8	24.5	77.8
AP CrB	AM	-14.4	17.4	19.7	30.0	V379 Vir	AM	16.7	-28.9	-15.1	36.6
V654 Aur	AM	13.1	10.5	13.8	21.7	IW Eri	AM	66.2	7.2	-41.2	78.4
J0859 + 0536	AM	33.6	-2.9	16.8	37.7	J1250 + 1549	AM	-10.4	-40.6	0.0	41.9
QS Tel	AM	-7.9	0.1	-24.5	25.8	J0425 – 5714	AM	-41.2	13.5	10.0	44.5
V516 Pup	AM	-43.1	20.8	4.4	48.0	GQ Mus	AM	-93.8	-39.0	-1.2	101.6
V381 Vel	AM	37.1	11.1	-11.9	40.6	J0921 + 2038	AM	-24.9	27.9	-19.5	42.2
V1189 Her	AM	-8.5	-22.4	50.4	55.8	BM CrB	AM	18.6	3.8	9.8	21.3
UW Pic	AM	-5.5	13.5	14.5	20.5	IL Leo	AM	15.7	-59.5	-18.3	64.2
J1333 + 1437	AM	-188.3	-108.3	50.6	223.0	EF Eri	AM	-15.9	-85.4	55.4	103.1
HU Leo	AM	-32.6	41.5	-7.4	53.3	J0154 – 5947	AM	28.0	14.6	10.4	33.2
J2218 + 1925	AM	28.1	3.3	-5.0	28.8	J0528 + 2838	AM	7.6	-46.9	17.8	50.7
MT Dra	AM	-26.7	16.9	6.5	32.3	GG Leo	AM	-20.6	5.2	-15.2	26.2
UZ For	AM	1.6	-0.7	18.7	18.8	EV UMa	AM	-11.5	-16.9	15.7	25.8
J2218 + 1925	AM	5.6	-5.5	14.5	16.5	V4738 Sgr	AM	12.9	16.9	11.2	24.0
EU Cnc	AM	-2.3	8.6	-13.8	16.4	J2340 + 7642	AM?	-36.4	-9.5	-1.2	37.6
HU Aqr	AM	74.1	-32.8	26.9	85.4	J0759 + 1914	AM?	25.3	-0.4	27.2	37.1
J1743 – 0429	AM	19.6	7.5	-22.3	30.7	J0935 + 1619	AM?	3.1	-35.8	-29.4	46.5
J0328 + 0522	AM	27.0	-4.8	-13.8	30.7	CP Pup	AM?	-0.4	16.8	6.7	18.1
V2951 Oph	AM	24.9	-1.0	-11.7	27.6	J0311 – 3152	AM?	34.8	-14.8	10.6	39.2
V808 Aur	AM	0.3	10.0	-16.2	19.0	J1955 + 0045	AM?	22.6	-4.1	-1.9	23.1
V1237 Her	AM	46.1	7.2	-5.9	47.1	PT Per	AM?	7.4	10.2	0.8	12.7
AR UMa	AM	-22.9	0.2	-6.7	23.8	J0354 – 1652	AM?	119.8	-84.9	-38.3	151.7
AN UMa	AM	-42.2	-46.0	-12.1	63.6						

Note. ^aIP - intermediate polar, IP? - intermediate polar candidate. AM - polar, AM? - polar candidate. The types of sources were obtained from Ritter & Kolb (2003) if there are no additional references. (1)Worpel et al. (2020), (2) Hilton et al. (2009), (3) Halpern & Thorstensen (2022), (4) Sambruna et al. (1992), (5) Kubiak & Krzeminski (1994), (6) Yakin et al. (2013), (7) Rosen et al. (1995), (8) Papadaki et al. (2006), (9) Zemko et al. (2018).

Table A2. Kinematical statistics of IPs and polars.

Type	Number	Component	Average	Dispersion
IP	57	<i>U</i>	6.4	34.4
		<i>V</i>	1.7	29.9
		<i>W</i>	0.9	19.9
		<i>T</i>	39.7	30.3
IP?	25	<i>U</i>	16.7	112.0
		<i>V</i>	-28.9	74.9
		<i>W</i>	-11.1	29.4
IP + IP?	82	<i>T</i>	88.7	110.0
		<i>U</i>	9.5	67.5
		<i>V</i>	-7.6	49.8
AM	99	<i>W</i>	-2.8	23.7
		<i>T</i>	54.6	68.8
		<i>U</i>	2.6	34.2
		<i>V</i>	-7.4	29.5
AM?	8	<i>W</i>	3.0	18.5
		<i>T</i>	40.4	28.4
		<i>U</i>	22.0	45.1
		<i>V</i>	-15.3	32.4
AM + AM?	107	<i>W</i>	-3.2	21.2
		<i>T</i>	45.8	44.4
		<i>U</i>	4.0	35.2
		<i>V</i>	-8.0	29.7
		<i>W</i>	2.5	18.7
		<i>T</i>	40.8	29.6

This paper has been typeset from a $\text{\TeX}/\text{\LaTeX}$ file prepared by the author.